

Defect Engineering of a High-Entropy Metallic Glass Surface for High-Performance Overall Water Splitting at Ampere-Level Current Densities

Xinyue Zhang, Yiyuan Yang, Yujing Liu, Zhe Jia,* Qianqian Wang, Ligang Sun,*
Lai-Chang Zhang, Jamie J. Kruzic, Jian Lu, and Baolong Shen*

Platinum-based electrocatalysts possess high water electrolysis activity and are essential components for hydrogen evolution reaction (HER). A major challenge, however, is how to break the cost-efficiency trade-off. Here, a novel defect engineering strategy is presented to construct a nanoporous (FeCoNiB_{0.75})₉₇Pt₃ (atomic %) high-entropy metallic glass (HEMG) with a nanocrystalline surface structure that contains large amounts of lattice distortion and stacking faults to achieve excellent electrocatalytic performance using only 3 at% of Pt. The defect-rich HEMG achieves ultralow overpotentials at ampere-level current density of 1000 mA cm⁻² for HER (104 mV) and oxygen evolution reaction (301 mV) under alkaline conditions, while retains a long-term durability exceeding 200 h at 100 mA cm⁻². Moreover, it only requires 81 and 122 mV to drive the current densities of 1000 and 100 mA cm⁻² for HER under acidic and neutral conditions, respectively. Modelling results reveal that lattice distortion and stacking fault defects help to optimize atomic configuration and modulate electronic interaction, while the surface nanoporous architecture provides abundant active sites, thus synergistically contributing to the reduced energy barrier for water electrolysis. This defect engineering approach combined with a HEMG design strategy is expected to be widely applicable for development of high-performance alloy catalysts.

1. Introduction

Hydrogen is a key pillar of decarbonization for our society.^[1] Considering its sustainability, high purity, and eco-friendly characteristics, water electrolysis is one of the most attractive targeted approaches for green hydrogen production.^[2] However, a major challenge for this technology is the development of low-cost and high-performance electrodes for anodic oxygen evolution reaction (OER) and cathodic hydrogen evolution reaction (HER).^[3] High-entropy alloys (HEAs), also referred to as compositionally complex alloys, have demonstrated great potential for the discovery of new catalysts owing to their wide and underexplored compositional space.^[4] The high-entropy feature of interest for catalysis is mainly associated with the compositionally complex sublattice occupation, which produces so-called “cocktail effects” or “compositionally synergistic effects.” Unlike binary ordered alloys, where each sublattice is occupied by a single element, two or more elements usually

X. Zhang, Y. Yang, Z. Jia, Q. Wang, B. Shen
School of Materials Science and Engineering
Jiangsu Key Laboratory for Advanced Metallic Materials
Southeast University
Nanjing 211189, China
E-mail: zhejia@seu.edu.cn; blshen@seu.edu.cn

Y. Liu
Institute of Metals
College of Materials Science and Engineering
Changsha University of Science & Technology
Changsha 410114, China

L. Sun
School of Science
Harbin Institute of Technology
Shenzhen 518055, China
E-mail: sunligang@hit.edu.cn

L.-C. Zhang
School of Engineering
Edith Cowan University
270 Joondalup Drive, Joondalup, Perth, WA 6027, Australia

J. J. Kruzic
School of Mechanical and Manufacturing Engineering
University of New South Wales (UNSW Sydney)
Sydney, NSW 2052, Australia

J. Lu
Hong Kong Branch of National Precious Metals Material Engineering
Research Center and Department of Mechanical Engineering
City University of Hong Kong
Hong Kong, SAR China

 The ORCID identification number(s) for the author(s) of this article can be found under <https://doi.org/10.1002/adma.202303439>

DOI: 10.1002/adma.202303439

occupy each sublattice of multicomponent HEAs. This introduces sublattice disordering with an increased configurational entropy, leading to unique atomic configurations that play an important role in improving the electrocatalytic behavior.^[4b] Inspired by such advances, great research efforts have been endeavored on developing novel types of HEAs for the purpose of electrocatalysis, e.g., those including high-entropy intermetallics (HEIs),^[5] eutectic dual-phase HEAs (EHEAs),^[6] as well as various groups of non-metallic compounds of high-entropy nitrides (HENSs),^[7] oxides (HEOs),^[8] sulfides (HESs),^[9] phosphides (HEPs),^[10] etc. However, state-of-the-art research on the development of HEA catalysts has mostly focused on the synergistic function from the multi-principal components. Other strategies for improving the electrocatalytic properties of HEAs, for example the use of lattice defects, have rarely been reported. More importantly, while defects such as lattice distortion (LD), stacking faults (SFs), and vacancies have been widely observed in HEA matrices due to the atomic size mismatch,^[11] to date it has been widely unknown how to promote such defects on the material surface to enhance electrocatalytic performance.

Metallic glasses (MGs) possess a disordered atomic packing structure that gives distinct differences in atomic and electronic structure compared to crystalline metallic alloys.^[12] Unlike the HEAs with a well-defined atomic structure, MGs possess high chemical homogeneity,^[13] high atomic diffusivity,^[14] and metastable nature^[15] that make them attractive templates for top-down surface modification, such as has been reported for the Ni-Zr-Ti-Pt,^[16] Pd-Ni-P,^[14] Pd-Cu-Ni,^[17] Pt-Ni-Cu-P,^[18] and Au-Cu-Si^[19] MGs. However, while tremendous research progress has been made in utilizing MG features such as high chemical homogeneity and atomic diffusivity to enable the fabrication of nanoporous architectures, the construction of surface defects through chemical dealloying is in fact limited by their single principal component design (i.e., other elements are minorly alloyed). While a high-entropy metallic glass (HEMG) approach has been shown to overcome this limitation, to date it has only been demonstrated with high amounts (e.g., 40 at%) of expensive noble metals.^[20]

In the present work, we demonstrate a novel defect engineering strategy to construct a nanoporous (FeCoNiB_{0.75})₉₇Pt₃ (atomic%) HEMG with a nanocrystalline surface structure that contains large amounts of LD and SF defects to achieve unsurpassed HER activity in pH-universal conditions and OER performance in the alkaline condition at ampere-level current densities compared to currently available catalysts that contain much higher amounts of expensive noble metals. By combining the benefits of the high-entropy concept with the chemical homogeneity of MGs, we achieve unsurpassed nanostructural control through surface reconstruction after electrochemical dealloying while the depletion of non-precious elements on surface greatly improves the utilization of a very small amount (3 at%) of Pt to break the cost-efficiency trade-off problem of previously developed water electrocatalysts. Finally, our structural and spectroscopic investigations reveal the mechanism for enhanced electrocatalytic performance is associated with LD and SF defects in the reconstructed nanocrystals that play key roles in optimizing the atomic coordination environment and modulating the electronic interaction.

2. Results and Discussion

Self-supported HEMG templates (Figure 1a) with an initial atomic composition of (FeCoNiB_{0.75})₉₇Pt₃ were prepared by a scalable and simple melt-spinning technique. Figure 1b shows an optical photograph of the as-spun (FeCoNiB_{0.75})₉₇Pt₃ HEMG. Electrochemical dealloying was employed by chronoamperometry method, where the voltage of -0.05 V (versus Ag/AgCl) was adopted in a 0.5 M H₂SO₄ solution to create the nanoporous surface architecture (Figure 1a; Figure S1, Supporting Information).^[21] The evolution of surface morphologies for the HEMG ribbon were confirmed by scanning electron microscopy (SEM) (Figure 1c–h) and atomic force microscope (AFM) (Figure 1i–n), respectively. It was found that the HEMG ribbon with a dealloying time of 150 s (DE 150 s) exhibited uniformly distributed nanopores on the free surface. Further increasing the dealloying time to 200 s (DE 200 s) was found to deteriorate the structural integrity of the ribbon making it brittle and prone to cracking (Figure S2, Supporting Information). To quantitatively determine the elemental variation on the HEMG surface, energy-dispersive X-ray spectroscopy (EDS) was employed for the HEMG ribbon at dealloying times of 0, 10, and 150 s (Figure S3, Supporting Information). It is noteworthy that the atomic concentration of Pt was sharply increased from 3.78% of the as-spun ribbon to 36.97% of the DE 150 s ribbon, thus promoting a better utilization of small amounts of Pt for the electrochemical reaction.

High-resolution transmission electron microscopy (HRTEM) of the as-spun HEMG ribbon showed a fully amorphous structure, which was also identified by diffuse diffraction rings in the selected area electron diffraction (SAED) patterns (Figure S4, Supporting Information). The cross-sectional microstructure of the DE 150 s HEMG ribbon was observed by spherical aberration-corrected high-angle annular dark-field scanning transmission electron microscopy (HAADF-STEM) (Figure 2a; Figure S5, Supporting Information). A 20–30 nm thick Pt-rich layer was clearly observed on the topmost surface. The high-resolution HAADF-STEM image of the Pt-rich layer confirmed the formation of nanocrystals during the dealloying process (Figure 2b). Crystalline interplanar spacings of the nanocrystals were measured to be 0.19 and 0.23 nm, corresponding to (200) and (111) planes for a face-centered cubic (FCC) structure, respectively. Moreover, an atom-stepped crystalline/amorphous interface was observed near the nanoporous region, which has been reported as beneficial to water electrolysis activity.^[22] More importantly, the nanocrystals in Figure 2b presented severe LD defects, which was also identified by the wavy lattice fringes in the inverse fast Fourier transform (IFFT) images (Figure 2c). The FFT image of the nanocrystalline region revealed that the nanocrystals were formed with interplanar spacings of 0.23, 0.19, and 0.14 nm for the (111), (200), and (220) crystal planes, respectively (Figure 2d), corroborating their FCC structure. Furthermore, the high-resolution HAADF-STEM characterization of the Pt-rich layer revealed an atomic structure with multiple SFs (Figure 2e), giving a high energy state that is often a key factor to promote catalytic performance.^[23] To confirm the compositionally complex sublattice occupation in the nanocrystals, atomic-level mapping results of Fe, Co, Ni, and Pt elements are shown in Figure 2f,g; Figure S6 (Supporting Information). The atomic pairs of Fe/Pt,

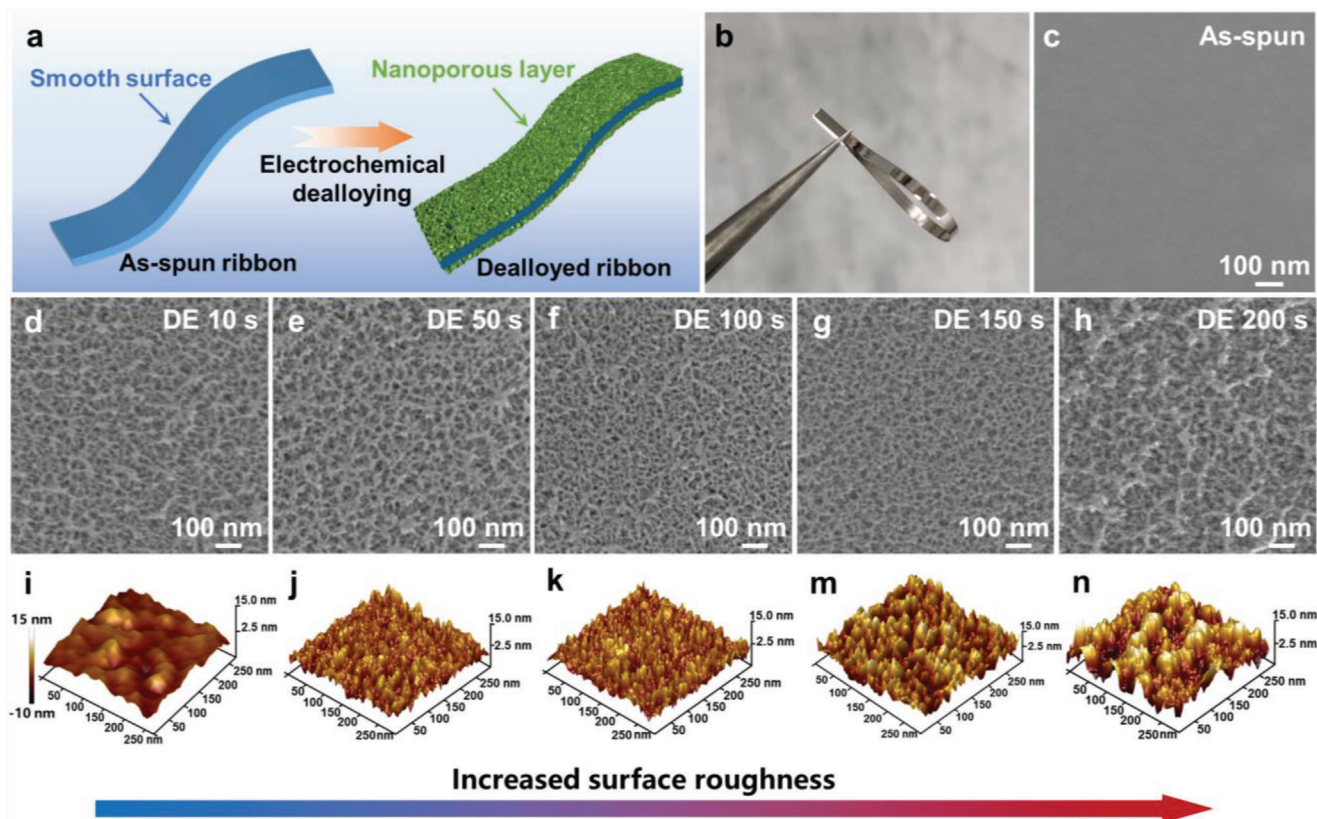


Figure 1. Conceptual design and surface characterization of the nanoporous $(\text{FeCoNiB}_{0.75})_{97}\text{Pt}_3$ HEMG. a) Schematic illustration of the preparation process of the nanoporous HEMG. b) Optical photograph of the as-spun $(\text{FeCoNiB}_{0.75})_{97}\text{Pt}_3$ HEMG. c) SEM image of the as-spun HEMG ribbon with smooth surface. d–n) SEM d–h) and AFM i–n) images of the dealloyed HEMG ribbons showing the nanoporous morphology.

Co/Pt, and Ni/Pt presented a homogeneous distribution, indicating the nanocrystalline phase was a chemically disordered solid solution, which was also verified by the EDS line-scan results in Figure 2h; Table S1 (Supporting Information). Moreover, Pt was highly concentrated in the nanocrystals at the topmost surface layer (≈ 50 at%) with a relatively low concentration of Fe, Co, and Ni (less than 20 at%), presenting a large compositional variation compared to the as-spun $(\text{FeCoNiB}_{0.75})_{97}\text{Pt}_3$ HEMG ribbon. One of the major functions of Fe, Co, and Ni was to be selectively dealloyed to form a homogeneously distributed nanopores on the topmost surface layer, which was mainly ascribed to the unique feature of the chemical homogeneity in MGs. For example, the porous/nanoporous morphology and distribution of other types of alloys are highly dependent on their phase structures and grain boundaries, but in MGs, the atoms are homogeneously distributed. The second function of Fe, Co, and Ni was to promote the formation of self-constructed nanocrystals around the nanopores, which was attributed to the high atomic diffusion rate and metastable nature of the glassy alloys. The loss of Fe, Co, and Ni would enhance the internal atomic diffusion from a metastable state (amorphization) to a relatively stable state (crystallization), which would be the possible reason for the formation mechanism of LD and SF in the nanocrystals in this work.

To determine the local coordination environment of Pt, we employed synchrotron-based X-ray absorption spectroscopy (XAS) (Figure 3). Figure 3a shows Pt L_3 -edge XANES spectra of

the as-spun and DE 150 s HEMG ribbons using Pt foil as a reference. The absorption energy of Pt for the as-spun and DE 150 s ribbons were close to that of the Pt foil, suggesting Pt mainly sit in metallic states.^[24] The extended X-ray absorption fine structure (EXAFS) spectrum of the DE 150 s ribbon exhibited close oscillation frequencies and amplitudes to the Pt foil compared to that of the as-spun ribbon (Figure 3b; Figure S7a–c, Supporting Information), demonstrating the electron coupling states around Pt atoms in the DE 150 s ribbon were similar to the Pt foil. This could be attributed to the large amount of Pt on the surface of the DE 150 s ribbon after electrochemical dealloying. The Fourier transform-EXAFS spectrum of the DE 150 s ribbon exhibited an obvious prominent peak at 2.760 Å, corresponding to the peak position of the Pt–Pt bond at 2.754 Å in Pt foil (Figure 3c; Figure S7d–f, Supporting Information). The slight shifting of the Pt–Pt bond in the DE 150 s ribbon was mainly attributed to a variation in the coordination environment of Pt with the elements of Fe, Co, and Ni, which was also evidenced by the peak shifting of the Pt–Pt bond for the as-spun ribbon. Wavelet transform of the k^3 -weighted Pt L_3 -edge EXAFS results revealed that the maximum peak intensity of the Pt–Pt bond in the DE 150 s ribbon was 8.9 \AA^{-1} , which was intermediate between the Pt foil and as-spun ribbon (Figure 3d–f). This could be attributed to a variation in the atomic coordination for the DE 150 s ribbon, which is in agreement with the XAS analysis. Table S2 (Supporting Information) summarizes the detailed structural parameters obtained from the

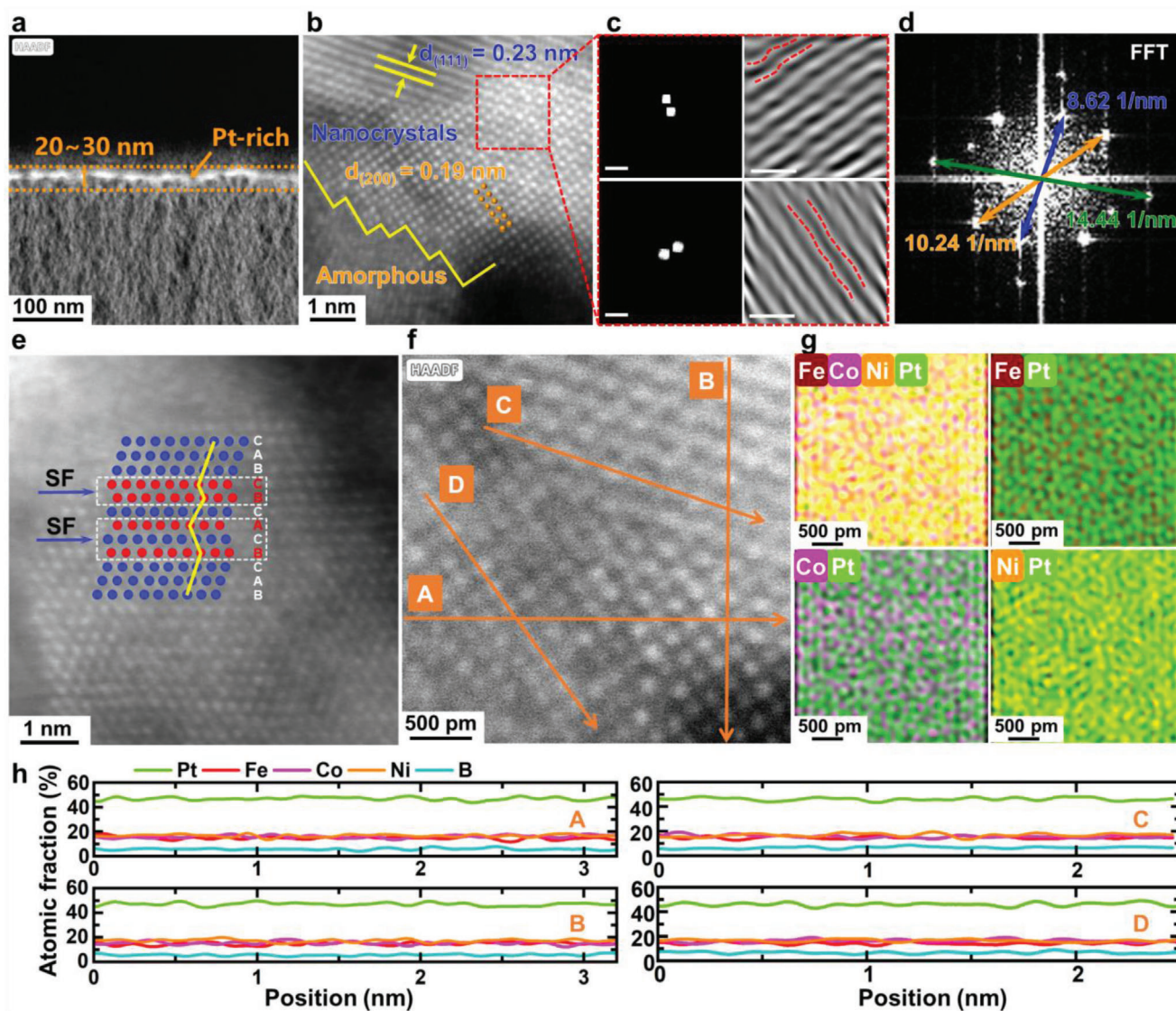


Figure 2. Structural characterization of the nanoporous $(\text{FeCoNiB}_{0.75})_{97}\text{Pt}_3$ HEMG. a) Cross-sectional HAADF-STEM image of the nanoporous HEMG showing a Pt-rich layer. b) High-resolution HAADF-STEM image in the Pt-rich nanocrystal region with LD. c) FFT and IFFT images of the red square frame region in b). The scale bars are 20 nm^{-1} and 0.5 nm for FFT and IFFT images respectively. d) FFT image of b). e) High-resolution HAADF-STEM image with SFs in the Pt-rich nanocrystal region. f) HAADF-STEM image, g) element mapping results, and h) line-scan results of the high-resolution Pt-rich nanocrystal region.

XAS analysis. The Pt atoms in the DE 150 s ribbon exhibited a decreased coordination number compared to that of the Pt foil and as-spun ribbon, indicating structural distortions and more dangling bonds occurred at the topmost surface.^[25]

X-ray photoelectron spectroscopy (XPS) was carried out to determine the surface chemical valence state of the samples (Figure S8, Supporting Information). Figure S8a (Supporting Information) shows Fe 2p high-resolution XPS spectra of the as-spun and DE 150 s ribbons, where the spectra consisted of three main peaks located at 706.8, 710.2, and 712.5 eV, corresponding to metallic Fe (Fe^0), Fe^{2+} , and Fe^{3+} , respectively.^[26] Co 2p XPS spectra could be deconvoluted into two peaks at 778.2 and 781.2 eV, which were assigned to the metallic Co (Co^0) and Co^{2+} , respectively (Figure S8b, Supporting Information). The binding

energies of Ni 2p XPS spectra at 852.6 and 855.8 eV were attributed to the metallic Ni (Ni^0) and Ni^{2+} , respectively (Figure S8c, Supporting Information). It was found that the Fe^0 , Co^0 , and Ni^0 peaks of the DE 150 s ribbon presented a much lower intensity compared to those of the as-spun ribbon, indicating the metallic Fe, Co, and Ni elements were gradually oxidized to higher valence states during the electrochemical dealloying process. The Pt 4f XPS spectrum of the as-spun ribbon exhibited a binding energy at 71.4 eV that could be assigned to metallic Pt (Pt^0) (Figure S8d, Supporting Information). While Pt^{2+} peaks were also observed for the DE 150 s ribbon, metallic Pt still played the dominant role on those surfaces. Such results are in good agreement with the characterization of metallic Pt from the XANES analysis (Figure 3a). The binding energies of B 1s XPS spectra at

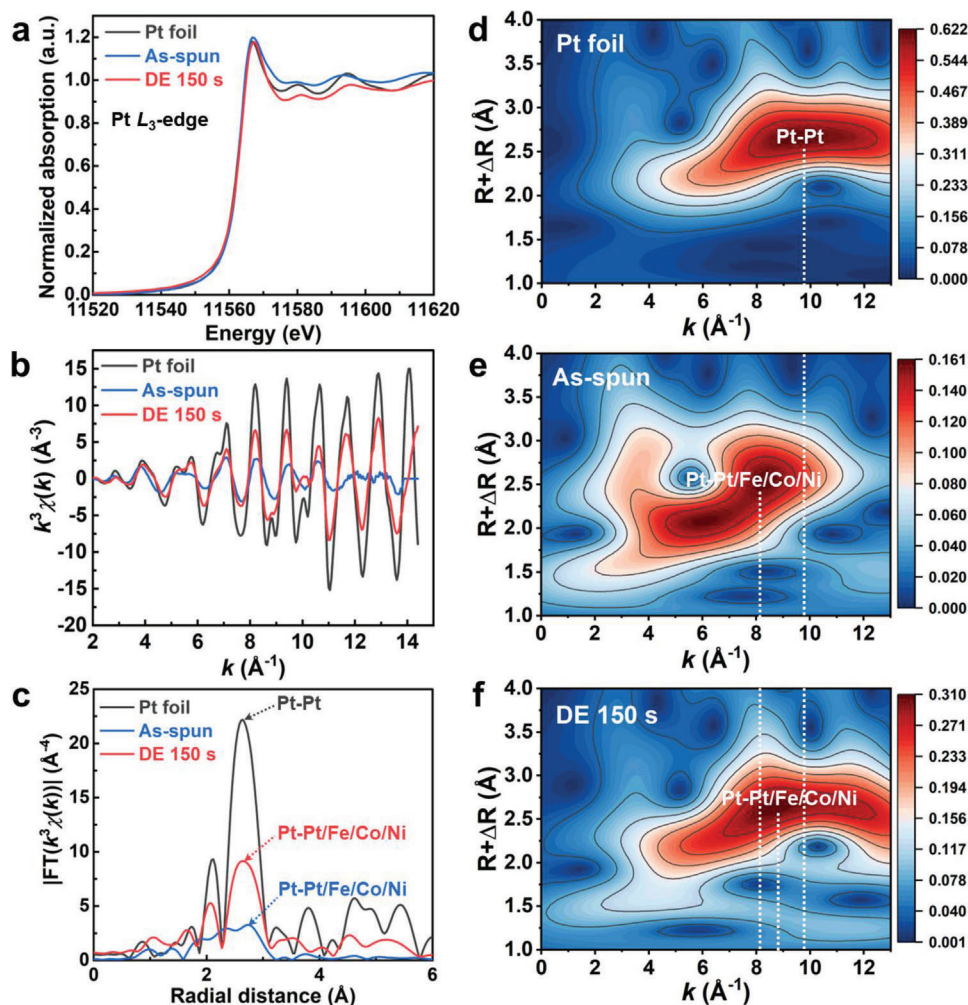


Figure 3. Electronic structure investigations. a) The normalized Pt L_3 -edge XANES spectra. b,c) The k^3 -weighted EXAFS oscillation b) and Fourier transform c) of the k^3 -weighted Pt L_3 -edge EXAFS spectra. d–f) Wavelet transform of the k^3 -weighted Pt L_3 -edge EXAFS results for Pt foil, as-spun, and DE 150 s ($\text{FeCoNiB}_{0.75}$) $_{97}$ Pt $_3$ HEMG.

187.8 and 191.4 eV were assigned to M–B and B–O bonds, respectively (Figure S8e, Supporting Information). The binding energies of O 1s XPS spectra could be deconvoluted into three peaks at 529.5, 531.2, and 532.9 eV, corresponding to O^{2-} , $-\text{OH}$, and adsorbed O, respectively (Figure S8f, Supporting Information). Surprisingly, it was found that the Co^{2+} , Ni^{2+} , and Pt^{2+} of the DE 150 s ribbon presented positive shifts compared to those of the as-spun ribbon, whereas the B–O bond and the peak positions of O 1s exhibited negative shifts. Such results suggested a variation in the atomic coordination environment and a strong electron hybridization phenomenon for the DE 150 s ribbon,^[27] which is in agreement with the above XANES analysis (Figure 3c–f).

The water electrolysis activities of the as-spun and dealloyed ribbons were investigated in pH-universal environments. In 1.0 M KOH solution, the DE 150 s ribbon exhibited an ultra-low overpotential of 170 mV to achieve a current density of 10 mA cm^{-2} for OER (Figure 4a), which was much lower than those of the as-spun $\text{FeCoNiB}_{0.75}$ HEMG (denoted as Pt $_0$, 374 mV, Figure S9a, Supporting Information), as-spun ($\text{FeCoNiB}_{0.75}$) $_{97}$ Pt $_3$ HEMG (denoted as Pt $_3$, 338 mV), DE 10 s (255 mV), DE 20 s

(239 mV), DE 50 s (205 mV), DE 100 s (200 mV), DE 200 s (183 mV), and DE 150 s Pt $_0$ (310 mV, Figure S9b, Supporting Information) ribbons as well as commercial RuO $_2$ nanoparticles (313 mV) which serve as a typical benchmark for OER activity comparison. Moreover, the DE 150 s ribbon also presented the smallest Tafel slope value of 37.8 mV dec^{-1} and a charge transfer resistance (R_{ct}) of 3.02Ω , indicating the fastest OER reaction kinetics and electron transfer ability compared to the other samples (Figure S10a–c, Supporting Information). With respect to the HER performance, the DE 150 s ribbon achieved an overpotential of 27 mV at the current density of 10 mA cm^{-2} , which was much lower than those of the Pt wire (91 mV), commercial Pt/C nanoparticles (71 mV), as-spun Pt $_0$ (469 mV), as-spun Pt $_3$ (350 mV), DE 10 s (51.7 mV), DE 20 s (47.8 mV), DE 50 s (42 mV), DE 100 s (38 mV), DE 200 s (29 mV), and DE 150 s Pt $_0$ (402 mV) ribbons (Figure 4b; Figure S9, Supporting Information). Figure S10d–f, Supporting Information shows the obtained values of Tafel slopes and R_{ct} , indicating that the DE 150 s ribbon has the best HER kinetics and electron transfer ability. Furthermore, the DE 150 s ribbon also presented a reliable sta-

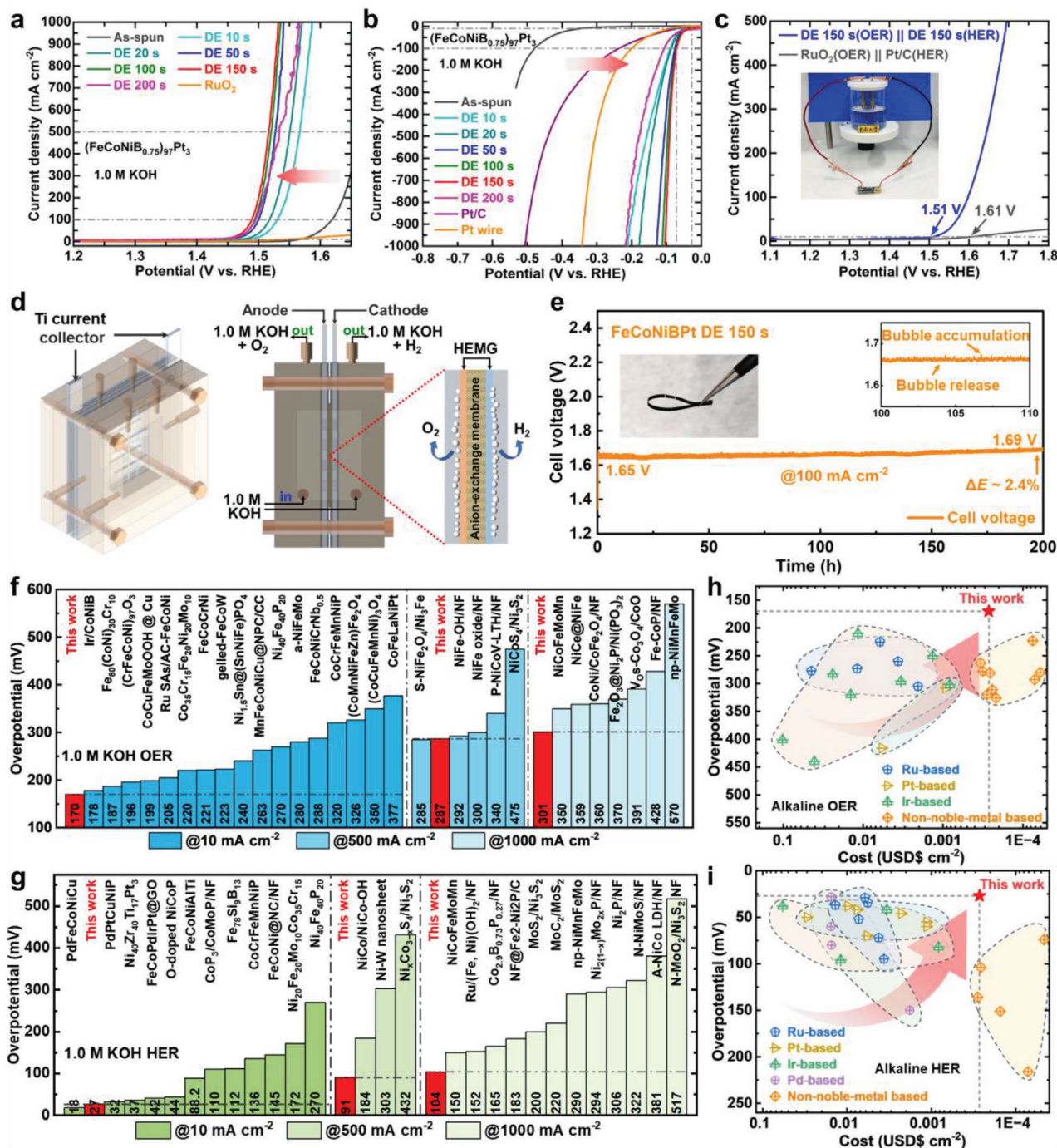


Figure 4. Electrochemical properties in an alkaline 1.0 M KOH solution. a, b) Polarization curves of OER a) and HER b) at a scan rate of 5 mV s^{-1} with iR loss correction. c) Overall water splitting polarization curves. d) Schematic diagram of DE 150 s HEMG || DE 150 s HEMG AEM electrolyser. e) Chronopotentiometry curve of the AEM electrolyser at a current density of 100 mA cm^{-2} without iR loss correction, the inset pictures showing the used HEMG ribbon and the enlarged view of stability curve. f–i) Comparison of OER f) and HER g) activity with recently reported electrocatalysts; comparison of raw material costs of various OER h) and HER i) electrocatalysts and their overpotentials at the current density of 10 mA cm^{-2} in 1.0 M KOH.

bility for 48 h at high current densities of 20 and 100 mA cm^{-2} with negligible elemental leaching (Figure S10g and Table S3, Supporting Information), suggesting their great potential for near-term commercialization. In light of such superior water electrolysis activity, we employed the DE 150 s ribbons as both

cathode and anode electrodes for overall water splitting in a dual-electrode system (Figure 4c). It only required a cell voltage of 1.51 V to drive the current density of 10 mA cm^{-2} , which is much lower than the cell voltage of 1.61 V for the RuO_2 || Pt/C dual-electrode system. To test the viability of DE 150 s HEMG

for large-scale hydrogen production, a flow-type anion-exchange membrane (AEM) electrolyser was assembled using DE 150 s HEMGs as both the anode and cathode (Figure 4d). It is noteworthy that the DE 150 s HEMG||DE 150 s HEMG AEM electrolyser delivered a current density of 100 mA cm⁻² at a cell voltage of only 1.65 V, and presented negligible cell voltage increase for 200 h. Moreover, the DE 150 s HEMG ribbon could maintain the integrality and flexibility after 200 h test, confirming their great potential for commercialization (Figure 4e). Furthermore, the DE 150 s ribbon exhibited incomparable high-current-density activities, only 287 and 301 mV required for OER to drive current densities of 500 and 1000 mA cm⁻², respectively, outperforming most currently developed electrocatalysts (Figure 4f; Table S4, Supporting Information). Meanwhile, the DE 150 s ribbon exhibited 91 and 104 mV for HER at current densities of 500 and 1000 mA cm⁻², respectively. The HER performance comparison with other state-of-the-art electrocatalysts was summarized in Figure 4g; Table S5 (Supporting Information). To further emphasize the cost-efficiency trade-off relationship, we have summarized dozens of recently reported electrocatalysts for cost-performance comparison (Figure 4h,i; Table S6 and S7, Supporting Information). It was found that our DE 150 s HEMG ribbon presented better or very close electrocatalytic performance compared to the noble-metal-based electrocatalysts with much lower material cost. Moreover, although the cost of our DE 150 s ribbon was a little bit higher than those of the non-noble-metal-based electrocatalysts, its water electrolysis activity was many times higher than them. Thus, our DE 150 s HEMG electrocatalyst sits in a class of its own in Figure 4h,i; Table S6 and S7 (Supporting Information). Additionally, the long stability performance of our DE 150 s HEMG ribbon in the AEM electrolyser is also a critical factor for the cost estimation, which was not considered in this work.

With respect to the neutral and acidic conditions in 1.0 M phosphate buffered saline (PBS) and 0.5 M H₂SO₄ electrolytes, our nanoporous defect-rich HEMG ribbon also presented superior HER activity with reliable stability (Figure S11, Supporting Information). The displayed overpotentials of the DE 150 s ribbon were only 69 and 122 mV at the current densities of 10 and 100 mA cm⁻² under the neutral condition, which were far lower than those of the Pt wire and commercial Pt/C nanoparticles as well as other published reports (Figure S11a,b and Table S8, Supporting Information). The corresponding Tafel slopes and R_{ct} values of the various samples are shown in Figure S12a,b (Supporting Information), indicating the DE 150 s ribbon has the fastest reaction kinetics and smallest R_{ct} under the neutral condition. Figure S11c (Supporting Information) shows the HER performance of the different samples under the acidic condition. The obtained overpotentials of the DE 150 s ribbon were 41 and 81 mV at the current densities of 10 and 1000 mA cm⁻², surpassing most currently developed catalysts (Figure S11d and Table S9, Supporting Information). The cost-efficiency comparison of our HEMG ribbon and various electrocatalysts under neutral and acidic conditions is summarized in Figure S11e,f and Table S10 and S11 (Supporting Information). The corresponding Tafel slopes and R_{ct} values of the various samples are shown in Figure S12c,d (Supporting Information), indicating the fast reaction kinetics of DE 150 s ribbon under the acidic condition. Meanwhile, the overpotentials were not significantly amplified during the sta-

bility test in both neutral and acidic conditions (Figure S11g, Supporting Information). The double-layer capacitances (C_{dl}) of the as-prepared samples were carried out within the non-faradaic potential region (0.683–0.783 V versus RHE) at scan rates between 10 to 50 mV s⁻¹ (Figure S13a–g, Supporting Information). The obtained C_{dl} value of the DE 150 s ribbon was 28.4 mF cm⁻², which was 2184 times higher than that of the as-spun ribbon (0.013 mF cm⁻²) (Figure S13h, Supporting Information). While the C_{dl} value of the DE 200 s ribbon was slightly higher than that of the DE 150 s ribbon, its mechanical strength was severely deteriorated (Figure S2, Supporting Information). Moreover, the calculated electrochemical active surface area (ECSA) values also exhibited the same trend with the C_{dl} values (Figure S13i, Supporting Information), indicating the significant contribution of the nanoporous surface morphology to enhance the water electrolysis activity.

To highlight the excellent structural stability, we also investigated the microstructural evolution of the DE 150 s ribbon after HER and OER tests. Note that the XRD patterns of the used DE 150 s ribbon presented a broad diffuse diffraction peak that was close to that of the as-prepared DE 150 s sample (Figure S14a and S15a, Supporting Information). The nanoporous surface morphology of the as-prepared DE 150 s ribbon was well retained after 48 h HER and OER durability tests (Figure S14b,c and Figure S15b,c, Supporting Information). The HRTEM images with the corresponding SAED patterns of the used DE 150 s ribbon exhibited the obvious nanocrystalline structure, where the lattice space fringes of 0.19 and 0.22 nm were in agreement with the previously observed FCC structure of the as-prepared DE 150 s ribbon (Figure S14d–f and Figure S15d,e, Supporting Information). Moreover, the LD defects were also well maintained in the used DE 150 s ribbon after the stability tests (Figure S15f, Supporting Information). Such results further verified the excellent stability performance of our HEMG electrocatalysts. XPS characterization of the used DE 150 s ribbon was also performed to monitor the variation of chemical valent states (Figure S16, Supporting Information). It was found that the metallic states of Fe, Co, and Ni in the as-prepared DE 150 s ribbon were completely oxidized to higher valent states in the used DE 150 s ribbon after the HER and OER tests, while the proportion of hydroxides in the used DE 150 s ribbon was increased, suggesting that electron transportation occurred during the electrochemical reaction.^[28] The B 1s signals became invisible for both the used DE 150 s ribbons after the HER and OER tests. The probable reason is the formation of hydroxides/oxides on the surface during the electrochemical reaction, which would affect the detection of B, especially since the concentration of B was very low in the DE 150 s ribbon (6.16 at%, Table S1, Supporting Information).

To elaborate the structural origin of the superior water electrolysis activity, density functional theory (DFT) calculations were performed to reveal an atomic-scale understanding of our HEMGs. Typically, the LD defects in FeCoNiBPt nanocrystals could be attributed to the atomic size mismatch of metallic elements and the interstitial solid solution of B atoms. According to the above structural characterizations, a series of atomistic models were initially built followed by structural relaxation (Figure 5a). It is noteworthy that the addition of B into the FCC and SF structures led to a large increase of degree of LD (Δd) (Figure 5b), suggesting the severe LD of the nanocrystals in this

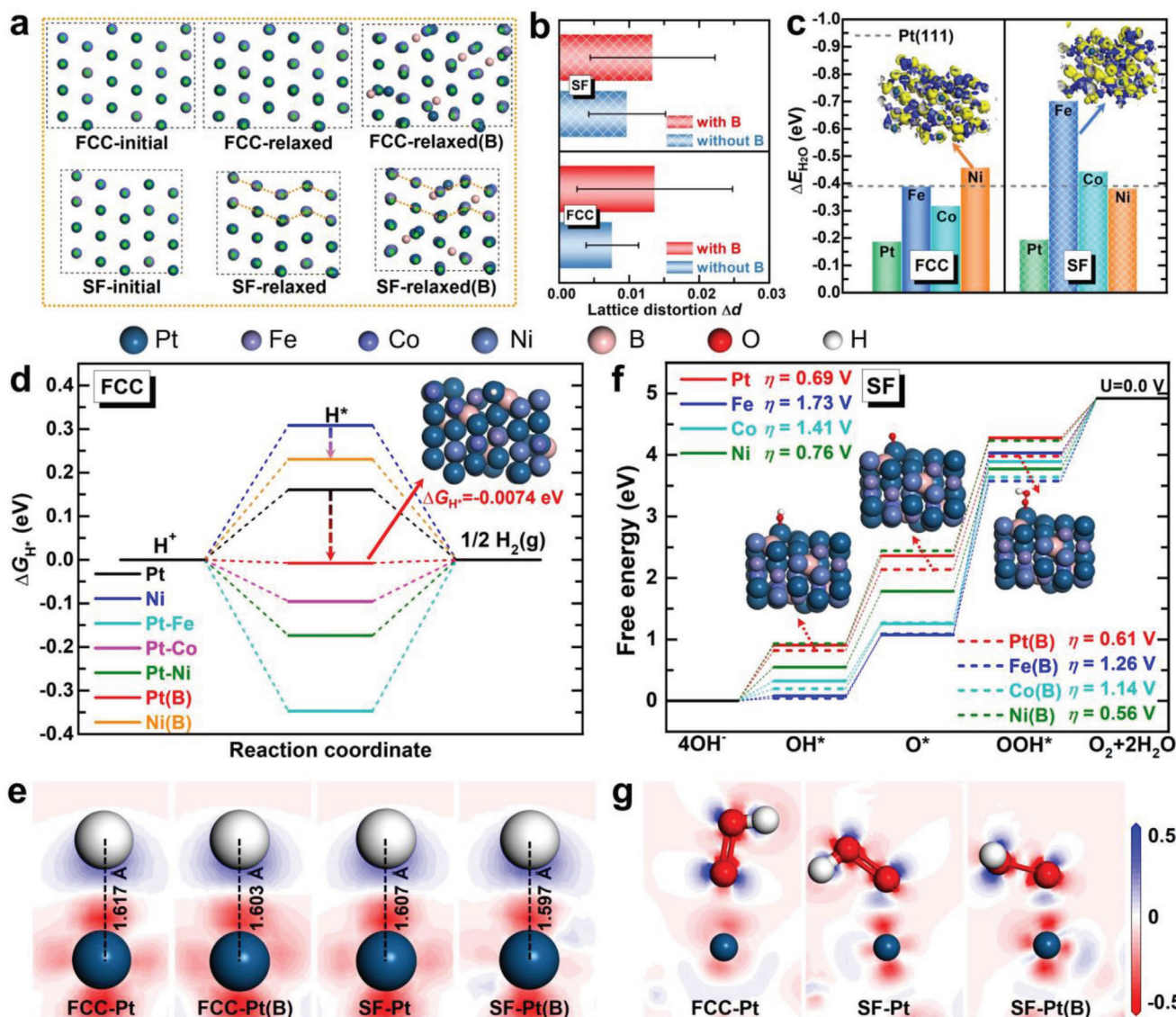


Figure 5. DFT simulation results. a) The atomic configurations of FCC and SF models. The green points mark the ideal lattice to highlight the LD effect. b) The degree of LD (Δd) of FCC and SF models with and without B. c) DFT calculated ΔE_{H_2O} for H_2O molecules adsorbed onto Pt, Fe, Co, and Ni sites in FCC and SF structural nanocrystals, respectively. As a reference, the ΔE_{H_2O} of the Pt (111) surface is marked by a grey dashed line. The inset images show the electron density differences of FCC-Ni and SF-Fe after H_2O adsorption. d) ΔG_{H^*} profiles on various catalytic sites in the FCC model. The dashed arrows highlight the change of ΔG_{H^*} after the active sites coordinated with B. e) DFT results of 2D electron density differences after adsorption of H^* onto FCC-Pt, FCC-Pt(B), SF-Pt, and SF-Pt(B) in the models. f) Free energy profiles of the single active sites with and without B with the SF structure at zero potential ($U = 0.0$ V). η represents the overpotential. The insets show the relaxed configurations with the adsorption of OH^* , O^* , and OOH^* intermediates at the SF-Pt(B) site. g) DFT results of 2D electron density differences after adsorption of OOH^* onto FCC-Pt, SF-Pt, and SF-Pt(B). Red and blue represent the depletion and accumulation of electrons with the unit of $e \text{ \AA}^{-3}$, respectively.

work was induced by B interstitial solid solution. Accordingly, to highlight the significant contribution of defects to the water electrolysis activity, four representative atomic models, including FCC and SF structures with and without interstitial solution of B atoms, were employed in this study. Figure S17 (Supporting Information) shows the atomic configurations and electron density differences at the Pt, Fe, Co, and Ni sites in the initial water adsorption step. The Fe and Co sites in the SF structure exhibited the highest H_2O adsorption energies (ΔE_{H_2O}) of -0.70 and -0.44 eV, which was much higher than that of the benchmark

of Pt (111) (Figure 5c). More details on ΔE_{H_2O} at various active sites in the FCC and SF structures are summarized in Table S12 (Supporting Information). To better elucidate the effects of LD on H_2O adsorption, we also compared the ΔE_{H_2O} for the active sites that coordinated with and without B atoms (Figure S18, Supporting Information). It is clear that the Pt and Ni sites with B coordination presented a larger ΔE_{H_2O} than the sites without B coordination, indicating the LD induced by interstitial B atoms was a contributing factor to the elevated ΔE_{H_2O} . Figure S19 (Supporting Information) shows the local 2D electron density

differences after H₂O adsorption onto these active sites. The darker red and blue color around the Pt(B) and Ni(B) sites as well as the O atoms indicated a stronger ability of electron depletion and accumulation, respectively. Moreover, the *p*-orbitals of O atom presented a left shift farther from the Fermi level (*E_F*) for the Pt(B) and Ni(B) sites (Figure S20, Supporting Information). Such results revealed the physical origin on the improvement of ΔE_{H_2O} for our defect-rich HEMG catalysts.

With respect to the HER performance, Gibbs free energy of H* (ΔG_{H^*}) was analyzed after H* adsorption at various active sites. Note that the ΔG_{H^*} is a key descriptor for the HER activity and a value close to zero indicates the interaction between active sites and H* is neither too strong nor too weak.^[29] Accordingly, a series of atomic configurations with stable H* adsorption along with their ΔG_{H^*} values are presented in Figure S21 and S22, Supporting Information. It is noteworthy that several high-performance active sites, such as Pt top, Pt-Co bridge, and Pt-Ni-Ni hollow sites, with favorable ΔG_{H^*} values were identified in the FCC and SF structural models (Figure 5d; Figure S23, Supporting Information). Particularly, the Pt site coordinated with B atoms presented favorable ΔG_{H^*} values of -0.0074 and 0.0312 eV that were closest to zero, indicating the significant effect of B coordination on the promotion of HER performance. To further uncover the effect of defects on the HER activity, we also compared the 2D electron density differences at various Pt sites in FCC and SF structures that were coordinated with and without B atoms (Figure 5e). It was found that the Pt(B) sites exhibited a favorable electron transferability with a shortened bonding distance of 1.603 and 1.597 Å compared to that of the Pt sites without B coordination. Furthermore, the *d*-band centers of the Pt(B) sites significantly shifted toward *E_F* suggesting the defects induced by interstitial B improve the interaction strength between H* and Pt sites (Figure S24, Supporting Information).

The atomistic mechanism for the excellent OER activity was also explored by DFT calculations. Specifically, the OER process at various active sites was investigated according to the four-electron transfer mechanism, and representative atomic configurations are presented in Figure S25 (Supporting Information) and inset of Figure 5f. The calculated free energy profiles are shown in Figure 5f; Figure S26 (Supporting Information) (*U* = 0.0 V), while the detailed free energies are listed in Table S13 and S14 (Supporting Information) (*U* = 0.0 V and *U* = 1.23 V). It was found that the rate-determining step (RDS) of the OER process for all active sites was the transition from O* to OOH*. Interestingly, the active sites in the SF structure achieved lower values of theoretical overpotential (η) than the sites in the FCC structure (Table S15, Supporting Information), suggesting the SF structure was more beneficial to the OER activity. With regards to the specific active sites, it was found that the obtained η values at the Pt and Ni sites ($\eta_{FCC-Pt} = 1.25$ V, $\eta_{SF-Pt} = 0.69$ V, $\eta_{SF-Pt(B)} = 0.61$ V, $\eta_{FCC-Ni} = 0.86$ V, $\eta_{SF-Ni} = 0.76$ V, $\eta_{SF-Ni(B)} = 0.56$ V) were much lower than those of the Fe and Co sites ($\eta_{FCC-Fe} = 2.25$ V, $\eta_{SF-Fe} = 1.73$ V, $\eta_{SF-Fe(B)} = 1.26$ V, $\eta_{FCC-Co} = 1.75$ V, $\eta_{SF-Co} = 1.41$ V, $\eta_{SF-Co(B)} = 1.14$ V). Although the Ni and Ni(B) active sites exhibited low η values, the low concentration of Ni (16.78 at%, Table S1, Supporting Information) on the nanoporous layer would limit its contribution to the OER activity. In comparison, it is noteworthy that the Pt and Pt(B) active sites possessed similar η values to the Ni and Ni(B) sites, while having a much higher concen-

tration on the nanoporous surface (46.55 at%), emphasizing the significant contribution of localized Pt enrichment to the promotion of water electrolysis performance. Moreover, the free energy profiles of possible bridge sites with different atomic pairs (Fe–Ni, Fe–Co, Fe–Pt, Pt–Ni, Pt–Co, and Ni–Co) were also calculated and the effect of B coordination was examined (Table S14 and S16, Supporting Information). Due to the low content of B (6.16 at%), all the bridge sites were regarded as coordinating with only one B atom. It is demonstrated that all the bridge sites exhibited weak OER performance with high RDS energy barriers ($\eta > 1.4$ V) although they could be slightly improved when a B atom simultaneously coordinated with both the metal atoms at the bridge sites ($\eta > 1.2$ V). Furthermore, to highlight the importance of defects on the improvement of the OER activity, we also compared the ΔG values for the active sites of SF-Pt and SF-Pt(B) (Figure 5f; Table S15, Supporting Information). It was found that the obtained ΔG_3 value (RDS, $\Delta G_3 = \Delta G_{OOH^*} - \Delta G_{O^*}$) of the SF-Pt(B) site was 1.84 eV, which was lower than that of the SF-Pt site (1.92 eV). These results suggest that the SF-Pt(B) site possessed a stronger electron-transfer ability toward OOH* (Figure 5g). Hence, the DFT results demonstrated that the defects of LD and SF structures induced by B element in the nanocrystals provide the most beneficial atomic configurations for water molecule adsorption, HER activity, and OER activity, providing an important defect engineering strategy for the design of excellent water electrocatalysts.

3. Conclusion

In summary, a novel defect engineering strategy was used to develop a nanoporous and defect-rich nanocrystalline surface structure within a (FeCoNiB_{0.75})₉₇Pt₃ HEMG to create a high-performance and low-cost electrocatalyst. Nanocrystals formed by partial dealloying are embedded around the nanopores on the HEMG surface and possess severe LD and many SFs that were induced by the interstitial B content, thus providing a large specific surface area with abundance of favorable active sites for superior water electrolysis performance. The developed defect-rich HEMG catalyst displays ultralow overpotentials at the ampere-level current density of 1 A cm⁻² for HER under pH-universal conditions and OER under alkaline condition, while it remains microstructurally stable with negligible elemental leaching and structural deterioration, outperforming that of commercial Pt/C and RuO₂ nanoparticles as well as other recently developed catalysts in the literature. The excellent performance is attributed to the following.

- 1) Partially dealloying of Fe, Co, and Ni gives rise to a sharp increase in the utilization of small amounts of Pt, while the nanoporous structure on the topmost surface of the HEMG ribbon provides an enlarged surface area for electrochemical reaction.
- 2) The self-constructed nanocrystals contain severe lattice distortion and many SFs that are promoted by the B element and that help optimize the water adsorption step and rate-determining steps of water electrolysis.
- 3) The multi-component synergistic function provides a variety of catalytic active sites.

The HEMG alloy design concept developed in this work is broad in scope and is expected to stimulate the discovery of many more high-performance catalytic materials that can be produced at industrial scale with customized properties in the future. Thus, we believe that our novel approach to compositionally complex alloy catalysts will define a new research field for developing next-generation environmentally friendly electrocatalyst materials that pave a new path for large-scale hydrogen generation.

Supporting Information

Supporting Information is available from the Wiley Online Library or from the author.

Acknowledgements

The authors acknowledge the support of Shanghai Synchrotron Radiation Facility for synchrotron-based X-ray absorption spectroscopy tests. This work was supported by the National Natural Science Foundation of China (Grant Nos. 52231005, 52201174, 12002108); Natural Science Foundation of Jiangsu Province (Grant No. BK20220858); Jiangsu Provincial Key Research and Development Program (Grant No. BE2021088); the Start-up Research Fund of Southeast University (RF1028623100); the Fundamental Research Funds for the Central Universities (2242023K5001, 2242023K40029); Guangdong Basic and Applied Basic Research Foundation (Grant No. 2020A1515110236, 2022A1515011402); Science, Technology, and Innovation Commission of Shenzhen Municipality (Grant No. ZDSYS2021061611000001).

Conflict of Interest

The authors declare no conflict of interest.

Author Contributions

Z.J., L.G.S., and B.L.S. designed the research; X.Y.Z., Y.J.L., Y.Y.Y., prepared and characterized the samples; Y.J.L. conducted TEM and HAADF-STEM characterizations; L.G.S. carried out DFT simulations; X.Y.Z., Z.J., L.G.S., L.C.Z., J.J.K., J.L., and B.L.S. analyzed the data and discussed the results; X.Y.Z., Z.J., L.G.S., and B.L.S. wrote the manuscript. All authors reviewed and contributed to the final manuscript.

Data Availability Statement

The data that support the findings of this study are available in the supplementary material of this article.

Keywords

defect engineering, high-entropy metallic glass, lattice distortion, stacking faults, water electrolysis

Received: April 13, 2023
Revised: May 24, 2023
Published online:

[1] a) J. A. Turner, *Science* **2004**, 305, 972; b) S. Chu, A. Majumdar, *Nature* **2012**, 488, 294.

- [2] X. Li, L. Zhao, J. Yu, X. Liu, X. Zhang, H. Liu, W. Zhou, *Nano-Micro Lett.* **2020**, 12, 131.
- [3] a) Z. P. Wu, X. F. Lu, S. Q. Zang, X. W. Lou, *Adv. Funct. Mater.* **2020**, 30, 1910274; b) G. Zhao, K. Rui, S. X. Dou, W. Sun, *Adv. Funct. Mater.* **2018**, 28, 1803291; c) Z. W. Seh, J. Kibsgaard, C. F. Dickens, I. B. Chorkendorff, J. K. Nørskov, T. F. Jaramillo, *Science* **2017**, 355, eaad4998.
- [4] a) J. W. Yeh, S. K. Chen, S. J. Lin, J. Y. Gan, T. S. Chin, T. T. Shun, C. H. Tsau, S. Y. Chang, *Adv. Eng. Mater.* **2004**, 6, 299; b) H. Li, J. Lai, Z. Li, L. Wang, *Adv. Funct. Mater.* **2021**, 31, 2106715; c) Y. F. Sun, S. Dai, *Sci. Adv.* **2021**, 7, eabg1600.
- [5] Z. Jia, T. Yang, L. Sun, Y. Zhao, W. Li, J. Luan, F. Lyu, L. C. Zhang, J. J. Kruzic, J. J. Kai, J. C. Huang, J. Lu, C. T. Liu, *Adv. Mater.* **2020**, 32, 2000385.
- [6] a) X. Han, Q. Chen, Q. Chen, Q. Wu, Z. Xu, T. Zheng, W. Li, D. Cui, Z. Duan, J. Zhang, J. Li, H. Li, Z. Wang, J. Wang, Z. Xia, *J. Mater. Chem. A* **2022**, 10, 11110; b) Z. Ding, J. Bian, S. Shuang, X. Liu, Y. Hu, C. Sun, Y. Yang, *Adv. Sustain. Syst.* **2020**, 4, 1900105.
- [7] T. Jin, X. Sang, R. R. Unocic, R. T. Kinch, X. Liu, J. Hu, H. Liu, S. Dai, *Adv. Mater.* **2018**, 30, 1707512.
- [8] a) Z. J. Chen, T. Zhang, X. Y. Gao, Y. J. Huang, X. H. Qin, Y. F. Wang, K. Zhao, X. Peng, C. Zhang, L. Liu, M. H. Zeng, H. B. Yu, *Adv. Mater.* **2021**, 33, 2101845; b) A. Abdelhafiz, B. Wang, A. R. Harutyunyan, J. Li, *Adv. Energy Mater.* **2022**, 12, 2200742.
- [9] T. X. Nguyen, Y. H. Su, C. C. Lin, J. M. Ting, *Adv. Funct. Mater.* **2021**, 31, 2106229.
- [10] a) D. Lai, Q. Kang, F. Gao, Q. Lu, *J. Mater. Chem. A* **2021**, 9, 17913; b) X. Zhao, Z. Xue, W. Chen, Y. Wang, T. Mu, *ChemSusChem* **2020**, 13, 2038.
- [11] Q. F. He, J. G. Wang, H. A. Chen, Z. Y. Ding, Z. Q. Zhou, L. H. Xiong, J. H. Luan, J. M. Pelletier, J. C. Qiao, Q. Wang, L. L. Fan, Y. Ren, Q. S. Zeng, C. T. Liu, C. W. Pao, D. J. Srolovitz, Y. Yang, *Nature* **2022**, 602, 251.
- [12] a) W. H. Wang, *Prog. Mater. Sci.* **2019**, 106, 100561; b) J. C. Qiao, Q. Wang, J. M. Pelletier, H. Kato, R. Casalini, D. Crespo, E. Pineda, Y. Yao, Y. Yang, *Prog. Mater. Sci.* **2019**, 104, 250; c) L.-C. Zhang, Z. Jia, F. Lyu, S.-X. Liang, J. Lu, *Prog. Mater. Sci.* **2019**, 105, 100576; d) F.-Y. Gao, S.-N. Liu, J.-C. Ge, X.-L. Zhang, L. Zhu, Y.-R. Zheng, Y. Duan, S. Qin, W. Dong, X. Yu, R.-C. Bao, P.-P. Yang, Z.-Z. Niu, Z.-G. Ding, W. Liu, S. Lan, M.-R. Gao, Y. Yan, S.-H. Yu, *Nat. Catal.* **2022**, 5, 993.
- [13] Y. Tan, F. Zhu, H. Wang, Y. Tian, A. Hirata, T. Fujita, M. Chen, *Adv. Mater. Interfaces* **2017**, 4, 1601086.
- [14] J. Yu, Y. Ding, C. Xu, A. Inoue, T. Sakurai, M. Chen, *Chem. Mater.* **2008**, 20, 4548.
- [15] Y. C. Hu, Y. Z. Wang, R. Su, C. R. Cao, F. Li, C. W. Sun, Y. Yang, P. F. Guan, D. W. Ding, Z. L. Wang, W. H. Wang, *Adv. Mater.* **2016**, 28, 10293.
- [16] R. Li, X. Liu, R. Wu, J. Wang, Z. Li, K. C. Chan, H. Wang, Y. Wu, Z. Lu, *Adv. Mater.* **2019**, 31, 1904989.
- [17] X. Yang, W. Xu, S. Cao, S. Zhu, Y. Liang, Z. Cui, X. Yang, Z. Li, S. Wu, A. Inoue, L. Chen, *Appl. Catal. B* **2019**, 246, 156.
- [18] G. Doubek, R. C. Sekol, J. Li, W.-H. Ryu, F. S. Gittleson, S. Nejati, E. Moy, C. Reid, M. Carmo, M. Linardi, P. Bordeenithikasem, E. Kinser, Y. Liu, X. Tong, C. O. Osuji, J. Schroers, S. Mukherjee, A. D. Taylor, *Adv. Mater.* **2016**, 28, 1940.
- [19] Y. Xu, J. Cheng, P. M. Yiu, G. Shan, T. Shibayama, S. Watanabe, M. Ohnuma, C.-H. Shek, *Nanoscale* **2018**, 10, 18846.
- [20] Z. Jia, K. Nomoto, Q. Wang, C. Kong, L. Sun, L. C. Zhang, S. X. Liang, J. Lu, J. J. Kruzic, *Adv. Funct. Mater.* **2021**, 31, 2101586.
- [21] a) J. Jayaraj, B. J. Park, D. H. Kim, W. T. Kim, E. Fleury, *Scr. Mater.* **2006**, 55, 1063; b) E. M. Paschalidou, F. Celegato, F. Scaglione, P. Rizzi, L. Battezzati, A. Gebert, S. Oswald, U. Wolff, L. Mihaylov, T. Spassov, *Acta Mater.* **2016**, 119, 177.

- [22] R. Li, R. Wu, Z. Li, J. Wang, X. Liu, Y. Wen, F. K. Chiang, S. W. Chen, K. C. Chan, Z. Lu, *Adv. Mater.* **2022**, 2206890, <https://doi.org/10.1002/adma.202206890>.
- [23] a) Y. Sun, K. Xu, Z. Wei, H. Li, T. Zhang, X. Li, W. Cai, J. Ma, H. J. Fan, Y. Li, *Adv. Mater.* **2018**, *30*, 1802121; b) C. Xia, Q. Jiang, C. Zhao, M. N. Hedhili, H. N. Alshareef, *Adv. Mater.* **2016**, *28*, 77.
- [24] T. Ma, H. Cao, S. Li, S. Cao, Z. Zhao, Z. Wu, R. Yan, C. Yang, Y. Wang, P. A. van Aken, L. Qiu, Y.-G. Wang, C. Cheng, *Adv. Mater.* **2022**, *34*, 2206368.
- [25] Y. Sun, S. Gao, F. Lei, Y. Xie, *Chem. Soc. Rev.* **2015**, *44*, 623.
- [26] Z. Jia, Y. Zhao, Q. Wang, F. Lyu, X. Tian, S. X. Liang, L. C. Zhang, J. Luan, Q. Wang, L. Sun, T. Yang, B. Shen, *ACS Appl. Mater. Interfaces* **2022**, *14*, 10288.
- [27] J. Liu, S. Zou, L. Xiao, J. Fan, *Catal. Sci. Technol.* **2014**, *4*, 441.
- [28] Q. Wang, Z. Jia, J. Li, Y. He, Y. Yang, Y. Li, L. Sun, B. Shen, *Small* **2022**, *18*, 2204135.
- [29] a) J. Greeley, T. F. Jaramillo, J. Bonde, I. B. Chorkendorff, J. K. Nørskov, *Nat. Mater.* **2006**, *5*, 909; b) J. K. Nørskov, T. Bligaard, A. Logadottir, J. R. Kitchin, J. G. Chen, S. Pandelov, U. Stimming, *J. Electrochem. Soc.* **2005**, *152*, J23.